PHOTONICS Research

Impact of non-Hermitian mode interaction on inter-cavity light transfer

Hyeon-Hye Yu,[1,†] Sunjae Gwak,[1,†] Jinhyeok Ryu,[1] Hyundong Kim,[1] Ji-Hwan Kim,[1] Jung-Wan Ryu,[2] Chil-Min Kim,[1,3] and Chang-Hwan Yi[2,4]

[1]Department of Emerging Materials Science, DGIST, Daegu 42988, Republic of Korea
[2]Center for Theoretical Physics of Complex Systems, Institute for Basic Science (IBS), Daejeon 34126, Republic of Korea
[3]e-mail: chmkim@dgist.ac.kr
[4]e-mail: yichanghwan@hanmail.net

Received 6 December 2021; revised 22 February 2022; accepted 10 March 2022; posted 14 March 2022 (Doc. ID 449515); published 14 April 2022

Understanding inter-site mutual mode interaction in coupled physical systems is essential to comprehend large compound systems, as this local interaction determines the successive multiple inter-site energy transfer efficiencies. In the present study, we demonstrate that only the non-Hermitian coupling can correctly account for the light transfer between two coupled optical cavities. We also reveal that the non-Hermitian coupling effect becomes crucial as the system dimension decreases. Our results provide important insight for handling general-coupled devices in the subwavelength regime.

https://doi.org/10.1364/PRJ.449515

1. INTRODUCTION

Pairwise-coupled systems have been an essential subject in almost all fields of physics, as they serve as the most foundational element to constitute large-scale complex systems. To date, coupled systems in various intrinsic physical states have been implemented in several fields such as hybrid quantum information [1–3], optical communication [4–6], and topological photonics [7–10]. A thorough understanding of the inter-site mutual mode couplings is vital for successful realizations of these systems.

As the cutting edge of modern technology reaches the realization of optoelectronic circuits, growing interest has been focused on coupled optical microcavities (COCs). Heretofore, numerous theoretical and experimental results have demonstrated their outstanding potential as efficient on-chip components. Because COCs can manipulate resonant modes and dispersions, they are used as optical delay lines [11–13], filters [14–17], and switches [18–20]. In addition, COCs have been considered as promising candidates for high-tech applications, for instance, optical memory [21–24], highly sensitive sensors [25–27], and single-mode lasers [28–30]. Recently, COCs have garnered newly increasing attention related to non-Hermitian physics [31,32], such as the non-Hermitian degeneracy so-called exceptional points (EPs) [33–35], parity–time symmetry [36–42], and photonic molecular states [43–51]. Up to now, most previous studies assume a lossless coupling between cavities [52–55] since the coupling loss is almost zero in the large-scale high-Q devices. However, as modern technology is challenging the sub-wavelength-scaled devices, it is necessary to understand the real coupling nature without the lossless coupling assumption in this regime.

2. INTER-CAVITY LIGHT TRANSFER

In this paper, we demonstrate that inter-cavity light transfer in the strong coupling regime [34] can only be explained correctly by lossy coupling between modes. As this coupling results in a fully non-Hermitian Hamiltonian for resonant modes [56], we refer to this lossy coupling as non-Hermitian couplingand lossless coupling as Hermitian coupling. To explicitly demonstrate the impact of non-Hermitian coupling in inter-cavity light transfer, we modeled two interacting whispering gallery modes (WGMs), each confined in different microdisks. We simulated experimental situations of inter-cavity light transfer through the time-dependent finite difference time domain (FDTD) method. The results were analyzed using the exact numerical results of the boundary element method (BEM) [57], as well as using the temporal coupled-mode theory (TCMT) [58,59]. Despite a number of previous works devoted to photonic-molecular WG-supermode [60–62], a critical non-Hermitian effect on the inter-cavity coupling has not been discovered in those works thus far. Recent experimental realizations of the coupled systems can be found, e.g., in Ref. [63].

Figure 1(a) is an illustration of our COCs, where two dielectric microdisks having radii of r_1 and r_2 are positioned at a distance of d_0. We set the refractive index as $n = 2.0$ inside the disks and as $n = 1.0$ outside the disks. We focus on

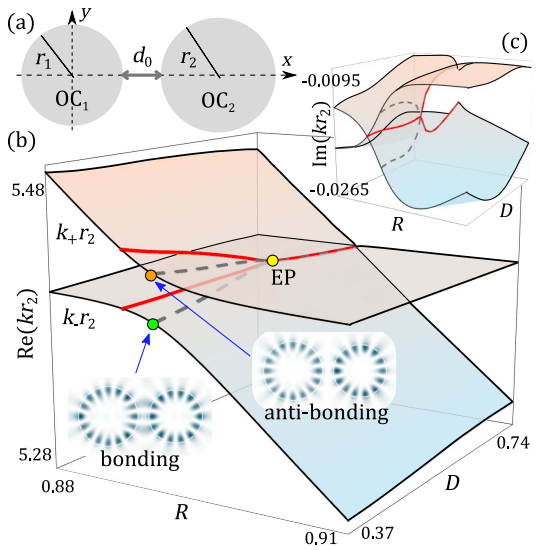

Fig. 1. (a) System configuration of coupled microcavities, where r_1 and r_2 are radii of cavities and d_0 is the inter-cavity distance. (b) and (c) are the Riemann surfaces for the real and imaginary parts of the resonant wavenumbers in the parameter space (R, D), obtained using the boundary element method. The branch-cut (interaction center) is marked by a red solid (gray dashed) curve. The insets in (b) are the spatial distributions of the two coupled modes at the interaction center.

transverse magnetic (TM) polarized WGMs. The insets in Fig. 1 depict two coupled modes that consist of two basis modes, WGM_1 and WGM_2, confined in each isolated OC_1 and OC_2. We have defined WGM_1 and WGM_2 by $(l, m) = (1,7)$ and $(1,8)$, where l and m represent radial and angular mode numbers, respectively. Throughout this paper, r_2 remains constant while two parameters $R \equiv r_1/r_2$ and $D \equiv d_0/r_2$ are used for constructing the Riemann surface: solution sets, $\{k\} \in \mathbb{C}$ (wavenumbers), of the Helmholtz equation, $-\nabla^2\psi(r) = n^2(r)k^2\psi(r)$, in the parameter space. Figures 1(b) and 1(c) examine the Riemann surface of coupled modes near $\mathrm{Re}(kr_2) = 5.5$ in $R \in [0.88,0.91]$ and $D \in [0.37,0.6]$ [64]. As used in the figure, we will employ the term "branch-cut" to refer to the coalescence curve of $\mathrm{Re}(kr_2)$ or $\mathrm{Im}(kr_2)$ in the parameter space.

We begin with FDTD calculations for the energy density of the steady-state (i.e., $t \to \infty$) electromagnetic fields in OC_1 and OC_2. In this numerical experiment, the COC is excited by two fundamental-TM mode sources, $e^{-i\omega t}$, located only in OC_2, where $i = \sqrt{-1}$, $\omega = ck_{\mathrm{in}} \in \mathbb{R}$, and c is the speed of light. Two sources located at the same position propagate bi-directionally (vertically upward/downward) along the cavity boundary with the same phase (see the arrows in the inset of Fig. 2) to excite the even-parity WGMs (see the insets in Fig. 1) about the horizontal axis. Figure 2 shows the normalized R-dependent energy density amplitude (EDA) defined [58] by

$$|a_j(k_{\mathrm{in}}r_2)| \equiv \frac{1}{|a_{\max}|}\left\{\frac{1}{2A_j}\int_{OC_j}[n^2(\mathbf{r})|E_j(\mathbf{r})|^2 + |B_j(\mathbf{r})|^2]\mathrm{d}\mathbf{r}\right\}^{\frac{1}{2}} \quad (1)$$

for a fixed $D = 0.37$, where A_j is the disk area of OC_j, E_j (B_j) is the electric (magnetic) field inside OC_j, and $|a_{\max}|$ is the normalization factor, which is the maximum EDA in the $(k_{\mathrm{in}}r_2, R)$ region of interest. The integral domain is restricted to the inside of the disk OC_j.

The EDA, $|a_1|$, in OC_1 can be interpreted as the light transfer efficiency from OC_2, as only the latter embeds the light source in it. In Fig. 2, it is found that the strongest light transfer occurs near a "interaction center" [≡, where the gap between $\mathrm{Re}(k_+r_2)$ and $\mathrm{Re}(k_-r_2)$ becomes the smallest, as shown in Fig. 1, respectively]. At this point, the two interacting modes form the well-known doublet of the bonding and anti-bonding photonic molecular states [43] (see Fig. 1), and they correspond to the lower (∇) and upper (Δ) triangles in Fig. 2(a). In the Fig. 2(a), as the solid vertical curve at $R = 0.892$ exhibits only a single peak over the anti-bonding mode (Δ), we can confirm that the light transfer associated with the anti-bonding mode is much stronger than that of the bonding mode.

To clarify the origin of this phenomenon, the EDA spectra were analyzed using a two-mode TCMT model of a evanescently coupled COC:

$$\begin{aligned}\frac{\mathrm{d}a_1}{\mathrm{d}t} &= -i\omega_1 a_1 - g_1 a_1 - i\gamma_{12}a_2,\\ \frac{\mathrm{d}a_2}{\mathrm{d}t} &= -i\omega_2 a_2 - g_2 a_2 - i\gamma_{21}a_1 + \sqrt{g_s}S_0 e^{-i\omega t},\end{aligned} \quad (2)$$

where $\omega_j \equiv c\,\mathrm{Re}(k_j)$ denotes the resonant frequency, $g_j \equiv c|\mathrm{Im}(k_j)|$ denotes the decay rate of WGM_j, and $\{a_j, S_0, \gamma_{ij}\} \in \mathbb{C}$ denotes the mode amplitude, source amplitude, and coupling coefficient, respectively. The validity of the two-mode approximation is guaranteed as the coupled modes are describable by the combination of WGM_1 and WGM_2, with negligible other low-Q mode contributions.

Given the time-harmonic ansatz of solutions, $a_j = a_j^0 e^{-i\omega t}$, we can obtain the steady-state amplitude $a_j^0 \in \mathbb{C}$ as follows:

$$\begin{aligned}a_1^0(\omega) &= \frac{-i\gamma_{12}\sqrt{g_s}S_0}{\gamma_{12}\gamma_{21} - (\omega - \omega_1 + ig_1)(\omega - \omega_2 + ig_2)},\\ a_2^0(\omega) &= \frac{-i\sqrt{g_s}S_0(\omega - \omega_1 + ig_1)}{\gamma_{12}\gamma_{21} - (\omega - \omega_1 + ig_1)(\omega - \omega_2 + ig_2)}.\end{aligned} \quad (3)$$

Essentially, a_1^0 and a_2^0 correspond to the FDTD results in Figs. 2(a) and 2(b), respectively. We emphasize that the coupling coefficients γ_{ij} in Eq. (3) are crucial for reproducing the FDTD experiments. Most importantly, it turns out that the typical assumption of a lossless coupling, $\gamma_{12} = \gamma_{21}^* \in \mathbb{C}$ or $\gamma_{12} = \gamma_{21} \in \mathbb{R}$ [58], is valid only in the classical limit $[\mathrm{Re}(kr_2) \gg 1]$ and may fail when approaching the subwavelength regime $[\mathrm{Re}(kr_2) \sim 1]$.

For an explicit demonstration of this finding, we set the effective Hamiltonian, which has complex wavenumber eigenvalues, $k_\pm \in \mathbb{C}$, of the coupled modes as follows:

$$\mathbf{H}_{\mathrm{eff}}\mathbf{c}^\pm = \begin{pmatrix} k_1 & \mu_{12} \\ \mu_{21} & k_2 \end{pmatrix}\begin{pmatrix} c_1^\pm \\ c_2^\pm \end{pmatrix} = k_\pm \begin{pmatrix} c_1^\pm \\ c_2^\pm \end{pmatrix}, \quad (4)$$

where $k_j \equiv (\omega_j - ig_j)/c$ represents complex wavenumbers of WGM_j with amplitudes $E_j(\mathbf{r})$ and $\mu_{ij} \equiv \gamma_{ij}/c$. The eigenvectors $(c_1^\pm, c_2^\pm)^{\mathrm{T}}$ are the coefficients of the two basis modes and construct new eigenstates of the coupled modes,

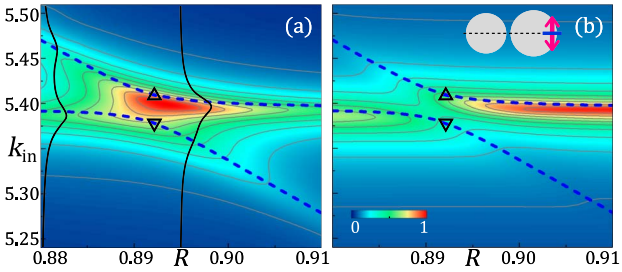

Fig. 2. (a) FDTD results of the EDA spectra of $|a_1|$ and (b) of $|a_2|$ at $D = 0.37$, as a function of (k_{in}, R). The dashed curves are $\mathrm{Re}(k_{\pm}r_2)$ obtained using the BEM. In (a), solid curves represent EDA as a function of k_{in} for fixed $R = 0.88$ and 0.892, whereas the upper/lower triangles mark the anti-bonding/bonding modes. The inset in (b) shows the radiating pumping source (arrow) used in FDTD simulation.

$E_{\pm}(\mathbf{r}) = c_1^{\pm}E_1(\mathbf{r}) + c_2^{\pm}E_2(\mathbf{r})$. For the known $k_{\pm}$, we can fix μ_{ij} after obtaining those coefficients numerically. By exploiting the general bi-orthogonality of modes in non-conservative systems, $\int n_i^2(\mathbf{r})E_i(\mathbf{r})\cdot E_j(\mathbf{r})d\mathbf{r} = \delta_{ij}$ [65,66], the coefficients are computed as follows:

$$c_i^{\pm} = \int n_i^2(\mathbf{r})E_i(\mathbf{r})\cdot E_{\pm}(\mathbf{r})d\mathbf{r}. \tag{5}$$

Hence, we can deduce a system of linear equations:

$$\begin{pmatrix} k_1 - k_{\pm} & \mu_{12} \\ \mu_{21} & k_2 - k_{\pm} \end{pmatrix}\begin{pmatrix} c_1^{\pm} \\ c_2^{\pm} \end{pmatrix} = 0, \tag{6}$$

for the unknowns k_j and μ_{ij}, respectively. Notably, we set k_j as free variables and $k_{\pm}$ as fixed values [67]. Eventually, the desired couplings μ_{ij} can be obtained as a function of the system parameters R and D. Figures 3(a) and 3(b) show the real and

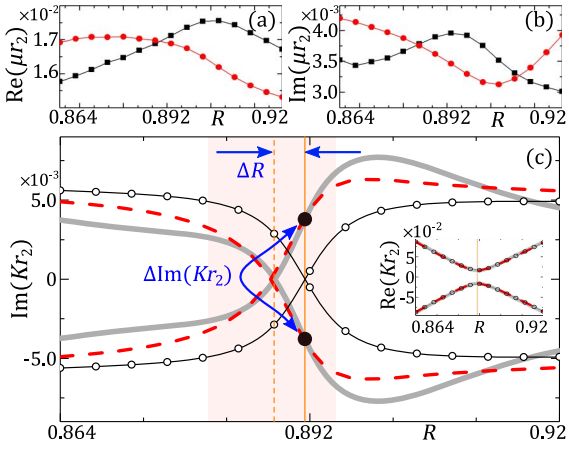

Fig. 3. Couplings of WGM_1 and WGM_2: (a) real and (b) imaginary parts of $\mu_{12}r_2$ (red circle) and $\mu_{21}r_2$ (black square) obtained using Eq. (6), as a function of R at $D = 0.37$. In (c), $\mathrm{Im}(K_{\pm}r_2)$ obtained using the BEM (gray solid) are compared to those obtained using Eq. (4) with the Hermitian (open circle) and non-Hermitian (red dashed line) couplings. The inset in (c) shows the $\mathrm{Re}(K_{\pm}r_2)$, where $K_{\pm}r_2$ are the re-expressed relative eigenvalues of the mean eigenvalues. The vertical solid lines in (c) and the inset mark the interaction center, whereas the vertical dashed line in (c) marks the branch-cut.

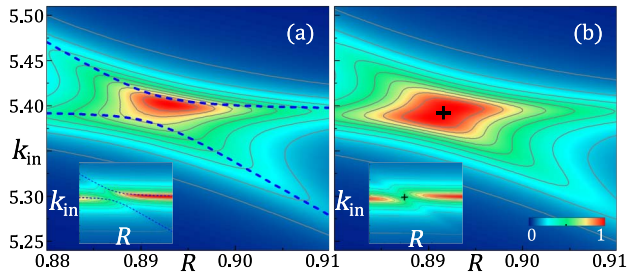

Fig. 4. TCMT results of the EDA spectra of $|a_1|$ with (a) true non-Hermitian and (b) artificial Hermitian couplings, respectively, at $D = 0.37$. The insets show the values of $|a_2|$. The dashed curves are $\mathrm{Re}(k_{\pm}r_2)$ obtained using the BEM.

imaginary parts of μ_{ij} as a function of R for a fixed $D = 0.37$. It is clear that $\mu_{12} \neq \mu_{21}^*$ in the regime of $kr_2 \sim 5$. Note that, as we can confirm that the single cavity modes always provide good approximations for the coupled-cavity modes obtained far from the interaction center, we can use them as basis functions for the coupled modes as well.

By inserting the obtained μ_{ij} into Eq. (3) through the relation $\mu_{ij} \equiv \gamma_{ij}/c$, we calculate the R-dependent $|a_1|$ at $D = 0.37$ in Fig. 4(a) ($|a_2|$ in the inset). These figures accurately reproduce the FDTD results shown in Fig. 2, in particular, enhanced light transfer near the anti-bonding mode. We can prove that this enhancement originates from the non-Hermitian couplings μ_{ij} through counter-exemplification of the artificial lossless coupling case, $\mu_{12} = \mu_{21}^* = (\mu_{12} + \mu_{21})/2$. As is depicted in Fig. 4(b) (and its inset), the Hermitian coupling yields a point-symmetric-like feature rather than an enhanced energy density near the anti-bonding mode.

3. EFFECT OF NON-HERMITIAN COUPLING

The effect of the non-Hermitian coupling described above can be understood as a consequence of a decay rate imbalance near the interaction center. Figure 3(c) and its inset show the imaginary and real parts of $K_{\pm}$ (≡ relative eigenvalues for the mean eigenvalue) that are obtained using a direct numerical method (BEM) and by solving Eq. (4) with the artificial Hermitian coupling, as well as the true non-Hermitian coupling. In the figures, although their real parts (inset) are almost identical, their imaginary parts show significant differences: the non-Hermitian coupling correctly reproduces the numerical results near the interaction center (shaded area), whereas the Hermitian coupling fails. More precisely, the non-Hermitian couplings reproduce the same shift of the branch-cut of the imaginary eigenvalues (ΔR) from the interaction center (solid orange line). The Hermitian coupling "never" induced this shift. Owing to this shift, the bonding and anti-bonding modes at the interaction center have distinctive decay rates [see the two big solid dots in Fig. 4(c)], long-lived anti-bonding modes, and short-lived bonding modes. Because the long-lived anti-bonding mode has a higher steady-state energy density in the cavity, it can provide a much more efficient light transfer route than the bonding mode.

The explanation for this decay rate imbalance is rather straightforward. Supposing the initial states with $\mathrm{Re}(k_1) = \mathrm{Re}(k_2)$

and $\mu_{12} = \mu_{21}^*$, then the difference between the two eigenvalues of Eq. (4) becomes

$$\Delta k \equiv k_+ - k_- = \sqrt{4|\mu_{12}|^2 - \mathrm{Im}(\delta k_{12})^2}, \quad (7)$$

where $\mathrm{Im}(\delta k_{12}) \equiv \mathrm{Im}(k_1 - k_2)$. Although $\mathrm{Im}(\delta k_{12})$ is independent of D, the coupling $|\mu_{12}|$ increases from zero to a finite value as D decreases from infinity. Accordingly, Δk changes from a pure imaginary value to a real number, that is, from a weak to strong coupling regime, via an EP, at which $4|\mu_{12}|^2 = \mathrm{Im}(\delta k_{12})^2$. In this Hermitian coupling case in the strong coupling regime, the interaction center and the point where $\mathrm{Im}(k_+) = \mathrm{Im}(k_-)$ (i.e., branch-cut) are identical in R variation for all D, that is, the lifetimes of the bonding and anti-bonding modes at the interaction center are the same, such that the point-symmetric-like feature of EDA in Fig. 4(b) is induced. In contrast to the Hermitian coupling case, however, if the coupling is lossy, that is, $\mu_{12} \neq \mu_{21}^*$, Δk in Eq. (7) becomes

$$\Delta k = \sqrt{4[(uu' - vv') + i(uv' + u'v)] - \mathrm{Im}(\delta k_{12})^2}, \quad (8)$$

where $\mu_{12} \equiv u + iv$, $\mu_{21} \equiv u' + iv'$, and $\{u^{(\prime)}, v^{(\prime)}\} \in \mathbb{R}$. We emphasize that the non-zero Im $(\mu_{12}\mu_{21}) = uv' + u'v$ shifts the branch-cut from the interaction center and splits the lifetimes of the doublet modes: long-lived anti-bonding and short-lived bonding modes at the interaction center. The shift direction of a branch-cut can be either to the right or left from the interaction center; therefore, the enhanced mode can be either the bonding or anti-bonding mode. Accordingly, the enhancement of the light transfer is independent of the wavefunction morphologies of the modes.

The branch-cut shift induced by the non-Hermitian coupling was found to be prominent in the subwavelength regime and diminished as we entered the classical regime. In Fig. 5(a), we obtain the parameter trajectories of the branch-cut and interaction center in the (R, D)-space for five different coupling pairs (i)–(v). In the Fig. 5(a), the defined mean wavenumbers $\equiv \mathrm{Re}(\langle k_1 + k_2 \rangle) r_2/2$ gradually increase from ∼3 to ∼8 for the pair from (i) to (v), where $\langle \cdot \rangle$ denotes the average over R. Clearly, the branch-cut shifts from the interaction center for smaller $\mathrm{Re}(kr_2)$ values, for instance, ∼3 for (i) is substantial, whereas it is negligible for larger values, such as ∼7 or 8 for (iv) and (v).

In fact, the transition from the non-Hermitian to the Hermitian coupling regime occurs very abruptly, much earlier than the classical regime, such as $\mathrm{Re}(kr_2) \sim 8$ in our examples. This abrupt transition is readily understood by the rapid convergence of $\mathrm{Im}(\mu_{12}\mu_{21})$ to zero as $\mathrm{Re}(kr_2)$ increases [see Eq. (8)]. In Fig. 5(b), we can observe that $|\mathrm{Im}(\langle \mu_{12}\mu_{21} \rangle)|$ is nearly zero for (v), whereas it is several orders of magnitude larger than (v) for (i). As the non-Hermitian coupling includes the "external coupling" via environments, this drastic effect of non-Hermitian coupling is profoundly associated with the openness [$\propto \mathrm{Im}(kr_2)$] of the involved modes. Note that the increased non-Hermitian coupling effect in the small cavity case demonstrates that the openness is a dominant factor giving rise to the non-Hermitian coupling, as the number of modes supported in the small-sized cavity is reduced significantly, i.e., the non-Hermitian coupling does not originate from the extra mode coupling effects. Because $\mathrm{Im}(\mu_{12}\mu_{21}) = uv' + u'v$ is a cross product of the real and imaginary parts of μ_{ij} [see Eq. (8)], the order of magnitude of $\mathrm{Im}(\mu_{12}\mu_{21})$ is determined by $|\mu_{ij}|$. As $|\mu_{ij}|$ is almost comparable to $|\mathrm{Im}(kr_2)|$ in Fig. 5(c), we can deduce that a larger decay of the basis mode results in stronger inter-site coupling. Therefore, we can conclude that the openness of basis modes directly promotes both the coupling strength itself and the non-Hermitian coupling effect, that is, a reduction in the confinement of the mode in the cavity leads to a higher impact of the non-Hermitian coupling. Our results can be viewed as being consistent with those in Ref. [68], which point out that the emission couplings and the evanescent couplings can be described differently by the skew-Hermitian and the Hermitian couplings, respectively.

Thus far, we have observed that the non-Hermitian coupling has a significant effect in general inter-cavity mode couplings when the basis modes are confined in non-identical disks with different angular momenta m. Here, we remark one special case [64]: inter-cavity couplings between the same m modes, $m_1 = m_2$, and $R \approx 1$. In Fig. 6, we examine the cases of $m = 7$ and $D = 0.37$. Owing to the symmetric property of R variation about $R = 1$, this COC has balanced values of

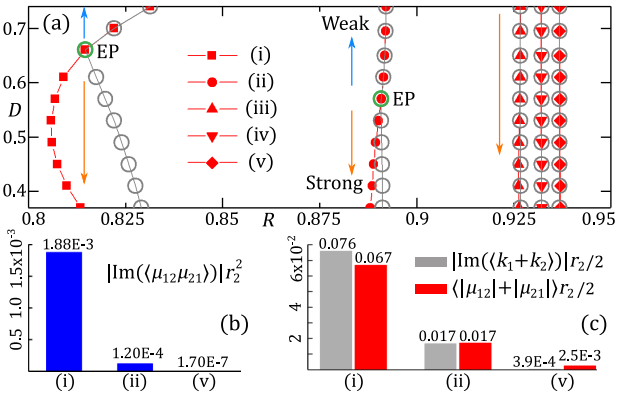

Fig. 5. (a) Parameter trajectory for the branch-cut (filled symbols) and the interaction center (open circles) for five cases of WGM coupling pairs defined by angular mode numbers: [(i), $(m_1, m_2) = (4,5)$], [(ii), (7,8)], [(iii), (11,12)], [(iv), (12,13)], [(v), (13,14)]. (b) $|\mathrm{Im}(\langle \mu_{12}\mu_{21} \rangle)|r_2^2$ for pairs (i), (ii), and (v) obtained at $D = 0.37$. (c) Comparison between the mean values of $\mathrm{Im}(kr_2)$ and μ_{ij} for the same pairs at $D = 0.37$.

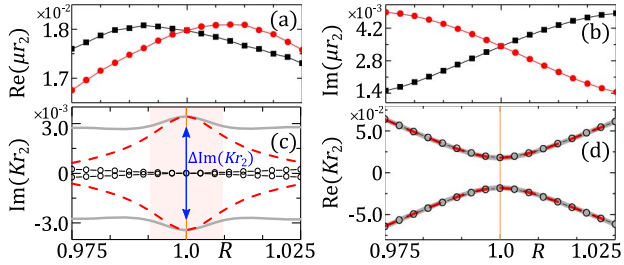

Fig. 6. Couplings for pair $(m_1, m_2) = (7,7)$, $R \approx 1$. (a) Real and (b) imaginary parts of $\mu_{12}r_2$ (red circle) and $\mu_{21}r_2$ (black square) obtained using Eq. (6), as a function of R at $D = 0.37$. The (c) real and (d) imaginary relative eigenvalues of $K_\pm r_2$ obtained using the BEM (gray solid) are compared to those obtained using Eq. (4) with the Hermitian (open circle) and non-Hermitian (red dashed) couplings. The vertical solid lines in (c) and (d) indicate the interaction center.

μ_{ij} [see Figs. 6(a) and 6(b)] and a definite interaction center; that is, it is not dependent on D at all [see Figs. 6(c) and 6(d)]. Moreover, there is no branch-cut in the Riemann surface; degeneracies in both $\mathrm{Re}(Kr_2)$ and $\mathrm{Im}(Kr_2)$ are always lifted at $R \approx 1$, provided that D is finite [64]. In Figs. 6(c) and 6(d), we find that while the non-Hermitian coupling reproduces this feature accurately, the Hermitian coupling is valid only for $\mathrm{Re}(Kr_2)$. The reason for this is exactly the same as before: as $\mathrm{Im}(\mu_{12}\mu_{21}) = 0$ through the definition of the Hermitian coupling, the split in $\mathrm{Im}(Kr_2)$ can never be realized, whereas the non-Hermitian coupling is able to realize this split. Therefore, again, the broken point symmetry in the EDA spectrum is induced (not shown) by the non-Hermitian coupling consistently in this system as well.

4. CONCLUSION

In summary, we have demonstrated that the inter-cavity light transfer can be explained successfully only when non-Hermitian coupling is considered. We also have found that the non-Hermitian coupling effect dramatically increases as the system size approaches the subwavelength regime. That is, the imaginary parts of coupling terms, inducing the branch-cut shift, are negligible when the system size is large; however, they increase rapidly as the system size decreases. This size-dependence effect of non-Hermitian coupling has been proven to be associated with the "opening" of modes. Recently, several theoretical models have utilized non-Hermitian coupling to achieve fruitful properties such as hierarchical EPs [69] and topological phase transition [10]. Substantiating these ideas to real devices can be accomplished only when we understand the genuine features of non-Hermitian couplings. In this regard, we believe our results will contribute to future technologies, such as on-chip silicon photonics and optoelectronic circuits [70,71] in the subwavelength regime where the non-Hermitian coupling effect becomes important.

Funding. National Research Foundation of Korea (NRF) (2021R1A2C1095623); Institute for Basic Science (IBS-R024-D1).

Acknowledgment. C.-H. Yi and J.-W. Ryu acknowledge financial support by IBS.

Disclosures. The authors declare no conflicts of interest.

Data Availability. Data underlying the results presented in this paper are not publicly available at this time but may be obtained from the authors upon reasonable request.

†These authors contributed equally to this work.

REFERENCES

1. Z.-L. Xiang, S. Ashhab, J. Q. You, and F. Nori, "Hybrid quantum circuits: superconducting circuits interacting with other quantum systems," Rev. Mod. Phys. **85**, 623–653 (2013).
2. S. Pirandola, J. Eisert, C. Weedbrook, A. Furusawa, and S. L. Braunstein, "Advances in quantum teleportation," Nat. Photonics **9**, 641–652 (2015).
3. Y. Li, W. Zhang, V. Tyberkevych, W.-K. Kwok, A. Hoffmann, and V. Novosad, "Hybrid magnonics: physics, circuits, and applications for coherent information processing," J. Appl. Phys. **128**, 130902 (2020).
4. J. K. Jang, A. Klenner, X. Ji, Y. Okawachi, M. Lipson, and A. L. Gaeta, "Synchronization of coupled optical microresonators," Nat. Photonics **12**, 688–693 (2018).
5. X. Xue, X. Zheng, and B. Zhou, "Super-efficient temporal solitons in mutually coupled optical cavities," Nat. Photonics **13**, 616–622 (2019).
6. W. Bogaerts, D. Pérez, J. Capmany, D. A. B. Miller, J. Poon, D. Englund, F. Morichetti, and A. Melloni, "Programmable photonic circuits," Nature **586**, 207–216 (2020).
7. T. Ozawa, H. M. Price, A. Amo, N. Goldman, M. Hafezi, L. Lu, M. C. Rechtsman, D. Schuster, J. Simon, O. Zilberberg, and I. Carusotto, "Topological photonics," Rev. Mod. Phys. **91**, 015006 (2019).
8. S. Malzard, C. Poli, and H. Schomerus, "Topologically protected defect states in open photonic systems with non-Hermitian charge-conjugation and parity-time symmetry," Phys. Rev. Lett. **115**, 200402 (2015).
9. H. Zhao, X. Qiao, T. Wu, B. Midya, S. Longhi, and L. Feng, "Non-Hermitian topological light steering," Science **365**, 1163–1166 (2019).
10. Y. Ao, X. Hu, Y. You, C. Lu, Y. Fu, X. Wang, and Q. Gong, "Topological phase transition in the non-Hermitian coupled resonator array," Phys. Rev. Lett. **125**, 013902 (2020).
11. J. E. Heebner and R. W. Boyd, "Slow and stopped light 'slow' and 'fast' light in resonator-coupled waveguides," J. Mod. Opt **49**, 2629–2636 (2002).
12. Y. Hara, T. Mukaiyama, K. Takeda, and M. Kuwata-Gonokami, "Heavy photon states in photonic chains of resonantly coupled cavities with supermonodispersive microspheres," Phys. Rev. Lett. **94**, 203905 (2005).
13. M. Hafezi, E. A. Demler, M. D. Lukin, and J. M. Taylor, "Robust optical delay lines with topological protection," Nat. Phys. **7**, 907–912 (2011).
14. B. E. Little, S. T. Chu, H. A. Haus, J. Foresi, and J. P. Laine, "Microring resonator channel dropping filters," J. Lightwave Technol. **15**, 998–1005 (1997).
15. S. Fan, P. R. Villeneuve, J. D. Joannopoulos, M. J. Khan, C. Manolatou, and H. A. Haus, "Theoretical analysis of channel drop tunneling processes," Phys. Rev. B **59**, 15882–15892 (1999).
16. C. M. Gentry and M. A. Popović, "Dark state lasers," Opt. Lett. **39**, 4136–4139 (2014).
17. H. Hodaei, A. U. Hassan, W. E. Hayenga, M. A. Miri, D. N. Christodoulides, and M. Khajavikhan, "Dark-state lasers: mode management using exceptional points," Opt. Lett. **41**, 3049–3052 (2016).
18. S. Pereira, P. Chak, and J. E. Sipe, "Gap-soliton switching in short microresonator structures," J. Opt. Soc. Am. B **19**, 2191–2202 (2002).
19. M. Soljačić, S. G. Johnson, S. Fan, M. Ibanescu, E. Ippen, and J. D. Joannopoulos, "Photonic-crystal slow-light enhancement of nonlinear phase sensitivity," J. Opt. Soc. Am. B **19**, 2052–2059 (2002).
20. K. Mukherjee and P. C. Jana, "Controlled optical bistability in parity-time-symmetric coupled micro-cavities: possibility of all-optical switching," Phys. E **117**, 113780 (2020).
21. M. T. Hill, H. J. S. Dorren, T. de Vries, X. J. M. Leijtens, J. H. den Besten, B. Smalbrugge, Y.-S. Oei, H. Binsma, G.-D. Khoe, and M. K. Smit, "A fast low-power optical memory based on coupled micro-ring lasers," Nature **432**, 206–209 (2004).
22. M. F. Yanik and S. Fan, "Stopping and storing light coherently," Phys. Rev. A **71**, 013803 (2005).
23. K. Totsuka, N. Kobayashi, and M. Tomita, "Slow light in coupled-resonator-induced transparency," Phys. Rev. Lett. **98**, 213904 (2007).
24. Q. Xu, P. Dong, and M. Lipson, "Breaking the delay-bandwidth limit in a photonic structure," Nat. Phys. **3**, 406–410 (2007).
25. J. Wiersig, "Enhancing the sensitivity of frequency and energy splitting detection by using exceptional points: application to microcavity sensors for single-particle detection," Phys. Rev. Lett. **112**, 203901 (2014).
26. W. Chen, Ş. K. Özdemir, G. Zhao, J. Wiersig, and L. Yang, "Exceptional points enhance sensing in an optical microcavity," Nature **548**, 192–196 (2017).
27. W. Chen, J. Zhang, B. Peng, Ş. K. Özdemir, X. Fan, and L. Yang, "Parity-time-symmetric whispering-gallery mode nanoparticle sensor," Photon. Res. **6**, A23–A30 (2018).

28. C. Zhang, C.-L. Zou, H. Dong, Y. Yan, J. Yao, and Y. S. Zhao, "Dual-color single-mode lasing in axially coupled organic nanowire resonators," Sci. Adv. **3**, e1700225 (2017).
29. W. Liu, M. Li, R. S. Guzzon, E. J. Norberg, J. S. Parker, M. Lu, L. A. Coldren, and J. Yao, "An integrated parity-time symmetric wavelength-tunable single-mode microring laser," Nat. Commun. **8**, 15389 (2017).
30. F. Gu, F. Xie, X. Lin, S. Linghu, W. Fang, H. Zeng, L. Tong, and S. Zhuang, "Single whispering-gallery mode lasing in polymer bottle microresonators via spatial pump engineering," Light Sci. Appl. **6**, e17061 (2017).
31. J. Okołowicz, M. Płoszajczak, and I. Rotter, "Dynamics of quantum systems embedded in a continuum," Phys. Rep. **374**, 271–383 (2003).
32. M. Hentschel, "Optical microcavities as quantum-chaotic model systems: openness makes the difference!" Adv. Solid State Phys. **48**, 293–304 (2009)..
33. T. Kato, *Perturbation Theory for Linear Operators* (Springer, 1966).
34. W. D. Heiss, "Repulsion of resonance states and exceptional points," Phys. Rev. E **61**, 929–932 (2000).
35. B. Peng, Ş. K. Özdemir, S. Rotter, H. Yilmaz, M. Liertzer, F. Monifi, C. M. Bender, F. Nori, and L. Yang, "Loss-induced suppression and revival of lasing," Science **346**, 328–332 (2014).
36. C. M. Bender and S. Boettcher, "Real spectra in non-Hermitian Hamiltonians having *PT* symmetry," Phys. Rev. Lett. **80**, 5243–5246 (1998).
37. R. El-Ganainy, K. G. Makris, D. N. Christodoulides, and Z. H. Musslimani, "Theory of coupled optical PT-symmetric structures," Opt. Lett. **32**, 2632–2634 (2007).
38. Ş. K. Özdemir, S. Rotter, F. Nori, and L. Yang, "Parity–time symmetry and exceptional points in photonics," Nat. Mater. **18**, 783–798 (2019).
39. H. Hodaei, M.-A. Miri, M. Heinrich, D. N. Christodoulides, and M. Khajavikhan, "Parity-time–symmetric microring lasers," Science **346**, 975–978 (2014).
40. L. Chang, X. Jiang, S. Hua, C. Yang, J. Wen, L. Jiang, G. Li, G. Wang, and M. Xiao, "Parity–time symmetry and variable optical isolation in active–passive-coupled microresonators," Nat. Photonics **8**, 524–529 (2014).
41. B. Peng, Ş. K. Özdemir, F. Lei, F. Monifi, M. Gianfreda, G. L. Long, S. Fan, F. Nori, C. M. Bender, and L. Yang, "Parity–time-symmetric whispering-gallery microcavities," Nat. Phys. **10**, 394–398 (2014).
42. J. Zhang, B. Peng, Ş. K. Özdemir, K. Pichler, D. O. Krimer, G. Zhao, F. Nori, Y.-X. Liu, S. Rotter, and L. Yang, "A phonon laser operating at an exceptional point," Nat. Photonics **12**, 479–484 (2018).
43. M. Bayer, T. Gutbrod, J. P. Reithmaier, A. Forchel, T. L. Reinecke, P. A. Knipp, A. A. Dremin, and V. D. Kulakovskii, "Optical modes in photonic molecules," Phys. Rev. Lett. **81**, 2582–2585 (1998).
44. T. Mukaiyama, K. Takeda, H. Miyazaki, Y. Jimba, and M. Kuwata-Gonokami, "Tight-binding photonic molecule modes of resonant bispheres," Phys. Rev. Lett. **82**, 4623–4626 (1999).
45. S. V. Boriskina, "Theoretical prediction of a dramatic *Q*-factor enhancement and degeneracy removal of whispering gallery modes in symmetrical photonic molecules," Opt. Lett. **31**, 338–340 (2006).
46. S. V. Boriskina, "Coupling of whispering-gallery modes in size-mismatched microdisk photonic molecules," Opt. Lett. **32**, 1557–1559 (2007).
47. M. Benyoucef, J.-B. Shim, J. Wiersig, and O. G. Schmidt, "Quality-factor enhancement of supermodes in coupled microdisks," Opt. Lett. **36**, 1317–1319 (2011).
48. R. El-Ganainy, M. Khajavikhan, and L. Ge, "Exceptional points and lasing self-termination in photonic molecules," Phys. Rev. A **90**, 013802 (2014).
49. M. Benyoucef, S. Kiravittaya, Y. F. Mei, A. Rastelli, and O. G. Schmidt, "Strongly coupled semiconductor microcavities: a route to couple artificial atoms over micrometric distances," Phys. Rev. B **77**, 035108 (2008).
50. N. Caselli, F. Intonti, F. La China, F. Biccari, F. Riboli, A. Gerardino, L. Li, E. H. Linfield, F. Pagliano, A. Fiore, and M. Gurioli, "Generalized Fano lineshapes reveal exceptional points in photonic molecules," Nat. Commun. **9**, 396 (2018).
51. M. Zhang, C. Wang, Y. Hu, A. Shams-Ansari, T. Ren, S. Fan, and M. Lončar, "Electronically programmable photonic molecule," Nat. Photonics **13**, 36–40 (2019).
52. H. A. Haus and W. Huang, "Coupled-mode theory," Proc. IEEE **79**, 1505–1518 (1991).
53. C. Manolatou, M. J. Khan, S. Fan, P. R. Villeneuve, H. A. Haus, and J. D. Joannopoulos, "Coupling of modes analysis of resonant channel add-drop filters," IEEE J. Quantum Electron. **35**, 1322–1331 (1999).
54. S. Deng, W. Cai, and V. N. Astratov, "Numerical study of light propagation via whispering gallery modes in microcylinder coupled resonator optical waveguides," Opt. Express **12**, 6468–6480 (2004).
55. C. Yang, Y. Hu, X. Jiang, and M. Xiao, "Analysis of a triple-cavity photonic molecule based on coupled-mode theory," Phys. Rev. A **95**, 033847 (2017).
56. J. Wiersig, "Formation of long-lived, scarlike modes near avoided resonance crossings in optical microcavities," Phys. Rev. Lett. **97**, 253901 (2006).
57. J. Wiersig, "Boundary element method for resonances in dielectric microcavities," J. Opt. A **5**, 53–60 (2003).
58. H. A. Haus, *Waves and Fields in Optoelectronics* (Prentice-Hall, 1984).
59. S. Fan, W. Suh, and J. D. Joannopoulos, "Temporal coupled-mode theory for the Fano resonance in optical resonators," J. Opt. Soc. Am. A **20**, 569–572 (2003).
60. A. I. Nosich, E. I. Smotrova, S. V. Boriskina, T. M. Benson, and P. Sewell, "Trends in microdisk laser research and linear optical modelling," Opt. Quantum Electron. **39**, 1253–1272 (2007).
61. C. Schmidt, A. Chipouline, T. Käsebier, E.-B. Kley, A. Tünnermann, T. Pertsch, V. Shuvayev, and L. Deych, "Observation of optical coupling in microdisk resonators," Phys. Rev. A **80**, 043841 (2009).
62. S. V. Boriskina, "Spectrally engineered photonic molecules as optical sensors with enhanced sensitivity: a proposal and numerical analysis," J. Opt. Soc. Am. B **23**, 1565–1573 (2006).
63. M. Parto, Y. G. Liu, B. Bahari, M. Khajavikhan, and D. N. Christodoulides, "Non-Hermitian and topological photonics: optics at an exceptional point," Nanophotonics **10**, 403–423 (2021).
64. J.-W. Ryu, S.-Y. Lee, and S. W. Kim, "Coupled nonidentical microdisks: avoided crossing of energy levels and unidirectional far-field emission," Phys. Rev. A **79**, 053858 (2009).
65. M. G. Raymer, "Quantum theory of light in a dispersive structured linear dielectric: a macroscopic Hamiltonian tutorial treatment," J. Mod. Opt. **67**, 196–212 (2020).
66. H. Eleuch and I. Rotter, "Clustering of exceptional points and dynamical phase transitions," Phys. Rev. A **93**, 042116 (2016).
67. J. Ryu, S. Gwak, J. Kim, H.-H. Yu, J.-H. Kim, J.-W. Lee, C.-H. Yi, and C.-M. Kim, "Hybridization of different types of exceptional points," Photon. Res. **7**, 1473–1478 (2019).
68. W. Suh, Z. Wang, and S. Fan, "Temporal coupled-mode theory and the presence of non-orthogonal modes in lossless multimode cavities," IEEE J. Quantum Electron. **40**, 1511–1518 (2004).
69. Q. Zhong, J. Kou, Ş. K. Özdemir, and R. El-Ganainy, "Hierarchical construction of higher-order exceptional points," Phys. Rev. Lett. **125**, 203602 (2020).
70. K. J. Vahala, "Optical microcavities," Nature **424**, 839–846 (2003).
71. D. K. Armani, T. J. Kippenberg, S. M. Spillane, and K. J. Vahala, "Ultra-high-*Q* toroid microcavity on a chip," Nature **421**, 925–928 (2003).